Microstructure and texture analysis of δ-hydride precipitation in Zircaloy-4 materials by electron microscopy and neutron diffraction

Zhiyang Wang,[a,b]* Ulf Garbe,[b] Huijun Li,[a] Yanbo Wang,[c] Andrew J. Studer,[b] Guangai Sun,[d] Robert P. Harrison,[e] Xiaozhou Liao,[c] M. A. Vicente Alvarez,[f] J. R. Santisteban[f] and Charlie Kong[g]

[a]Faculty of Engineering, University of Wollongong, Northfields Avenue, Wollongong, NSW 2522, Australia, [b]Bragg Institute, Australian Nuclear Science and Technology Organisation, New Illawarra Road, Lucas Heights, NSW 2234, Australia, [c]School of Aerospace, Mechanical and Mechatronic Engineering, University of Sydney, NSW 2006, Australia, [d]Institute of Nuclear Physics and Chemistry, CAEP, Mianyang 621900, People's Republic of China, [e]Institute of Materials Engineering, Australian Nuclear Science and Technology Organisation, New Illawarra Road, Lucas Heights, NSW 2234, Australia, [f]CONICET and Instituto Balseiro, Centro Atómico Bariloche, Argentina, and [g]Electron Microscope Unit, University of New South Wales, Sydney, NSW 2250, Australia. Correspondence e-mail: zw603@uowmail.edu.au

This work presents a detailed microstructure and texture study of various hydrided Zircaloy-4 materials by neutron diffraction and microscopy. The results show that the precipitated δ-$ZrH_{1.66}$ generally follows the $\delta(111)//\alpha(0001)$ and $\delta[1\bar{1}0]//\alpha[11\bar{2}0]$ orientation relationship with the α-Zr matrix. The δ-hydride displays a weak texture that is determined by the texture of the α-Zr matrix, and this dependence essentially originates from the observed orientation correlation between α-Zr and δ-hydride. Neutron diffraction line profile analysis and high-resolution transmission electron microscopy observations reveal a significant number of dislocations present in the δ-hydride, with an estimated average density one order of magnitude higher than that in the α-Zr matrix, which contributes to the accommodation of the substantial misfit strains associated with hydride precipitation in the α-Zr matrix. The present observations provide an insight into the behaviour of δ-hydride precipitation in zirconium alloys and may help with understanding the induced embrittling effect of hydrides.

1. Introduction

Hydride-induced embrittlement has been recognized as one of the most important reasons for failure in zirconium (Zr) alloys, which are core structural materials used extensively in nuclear reactors. Hydrogen ingress and subsequent hydride precipitation in Zr alloys under in-reactor service conditions are normally inevitable, mainly attributed to the strong affinity of Zr with hydrogen and the low solubility of hydrogen in the Zr matrix (less than 10 wt p.p.m. at room temperature; Kearns, 1967). Owing to the intrinsic brittleness of hydrides at low temperature, hydride formation may severely embrittle the Zr matrix, leading to substantial losses of ductility, and of impact and fracture toughness. When the concentration of hydride precipitates reaches a critical value, a slow crack-propagation process called delayed hydride cracking (DHC) may be initiated in Zr alloy components with certain levels of internal or external stress (Dutton et al., 1977; Puls, 1990; Shi et al., 1995). The initiation of DHC may gradually degrade the structural integrity of the components and thus reduce their useable lifetime. Because of the technological importance of this hydride-assisted cracking issue, the precipitation behaviour of

hydrides and their induced embrittlement of Zr alloys have been the subject of extensive research work (Bai, Ji et al., 1994; Bai, Prioul & François, 1994; Mani Krishna et al., 2006; Colas et al., 2010; Qin et al., 2011, 2012).

Previous results demonstrated that hydride precipitation in Zr alloys is a complicated process. The morphology, distribution and crystallographic features of hydrides are influenced by several factors, including the hydriding conditions and the matrix microstructure and texture (Nath et al., 1975; Bai, Prioul & François, 1994; Santisteban et al., 2010). For instance, the formation of the equilibrium face-centred cubic (f.c.c.) δ-hydride phase is favoured by slow cooling rates and high hydrogen contents, whereas the metastable face-centred tetragonal γ-hydride phase tends to precipitate under quenching conditions (Nath et al., 1975). The frequently reported orientation relationship (OR) of the δ-hydride with the α-Zr matrix is $\delta(111)//\alpha(0001)$, although some other crystallographic correlations [such as $\delta(111)//\alpha(10\bar{1}0)$] are occasionally observed. Qin et al. (2011) assumed that the various alloy compositions and hydrogen concentrations of hydrided Zr alloys used in different work may alter the

research papers

matching of atom patterns and spacings at the hydride–matrix interface and lead to variations in the OR. The δ-hydrides display a common acicular or platelet morphology, as seen in optical metallographic examinations, and transmission electron microscopy (TEM) observations revealed that optically visible hydrides are often composed of stacks of smaller hydrides which may have different crystallographic orientations (Perovic *et al.*, 1983). In addition, it is worth noting that δ-hydride precipitation is accompanied by a significant volume expansion (*i.e.* dilatational strain) that requires both elastic and plastic accommodation by the hydride and the surrounding α-Zr matrix during the hydride precipitation process (Carpenter, 1973; Puls, 1984; Lufrano *et al.*, 1998). The states of the internal stress in the δ-hydride precipitated in Zircaloy-4 (Zr-4) and Zr-2.5Nb alloys, generated as a result of the elastic accommodation behaviour, were evaluated in recent work by Santisteban and Vicente Alvarez and co-workers (Santisteban *et al.*, 2010; Vicente Alvarez *et al.*, 2012), uncovering the magnitude and nature of the stresses existing within hydrides. However, not much information about the response of the plastic accommodation (*e.g.* the generation of misfit dislocations) for hydride formation in Zr alloys is available in the open literature (Bai, Ji *et al.*, 1994), although this knowledge is needed for a better understanding of the subtle microstructural features and brittle characteristics of hydrides formed *in situ* in Zr alloys. Another concern is potential developments in the crystallographic texture of hydrides, taking into account the presence of α-Zr matrix texture produced in the thermomechanical processing steps of the material and the existing preferred OR between hydride and matrix. Several research works have reported hydride texture measured in hydrided Zr alloys using synchrotron X-ray diffraction (Santisteban *et al.*, 2010; Vicente Alvarez *et al.*, 2011, 2012) and neutron diffraction (Wang *et al.*, 2012). In order to shed some light on the general characteristics and origin of hydride texture, it might still be necessary to perform further texture analysis on both the hydride and matrix phases in various Zr alloys with apparently different matrix textures, and a comparison between the new results and those already reported would be of great interest.

In this work, we present a comprehensive microstructure and texture analysis on two hydrided Zr-4 materials containing high levels of hydrogen (∼2000 wt p.p.m.), primarily by neutron diffraction and electron microscopy. The bulk textures of the hydride and α-Zr matrix phases were determined in order to understand the characteristics and origin of hydride texture. Neutron diffraction line profile analysis combined with a high-resolution transmission electron microscopy (HRTEM) investigation was also performed, aiming to reveal the potential generation and distribution of misfit dislocations in the hydride and adjacent α-Zr matrix resulting from the plastic accommodation of the substantial dilatational strains associated with hydride transformation.

These detailed microstructure and texture observations reveal the general features of hydrides that are formed through the Zr → hydride transformation and embedded in a Zr-4 matrix. Extensive experimental information is obtained

Table 1
Chemical composition of Zircaloy-4 used in the present study.

Element	Sn	Fe	Cr	O	Zr
Content (wt%)	1.56	0.22	0.11	0.14	Balance

from this work, including the primary hydride–matrix crystallographic OR, the average dislocation density and the macroscopic texture of the hydrides. In particular, the origin and characteristics of hydride bulk texture, which were not completely understood before owing to the lack of specific studies of the macroscopic texture of hydrides precipitated in various Zr alloys with distinct textures, are clarified in this work *via* investigations of the hydride precipitation behaviours in different textured Zr-4 materials. The fundamental knowledge acquired is of great significance for understanding hydride precipitation behaviour and related embrittlement effects in Zr alloys. Additionally, although this study was not conducted under the application conditions of the material (high temperature, pressure and radiation), we believe that the observations and conclusions obtained here could still assist in understanding hydride formation and induced embrittlement in Zr alloys under the harsh reactor operating environment.

2. Experimental

2.1. Sample preparation

Commercial Zr-4 materials (ASTM grade R60804, purchased from Wah Chang, USA) in two thermal-mechanical states, *i.e.* hot-rolled and annealed plate (referred to as plate hereinafter), and hot-extruded and annealed round bar (referred to as bar), were used in this study; the chemical composition is given in Table 1. The Zr-4 plate was annealed in the range 1033–1083 K for 1.5 h and the bar treated at 973 K for 3 h, producing a relatively homogeneous microstructure characterized by equi-axial α-Zr grains with an average diameter of ∼10 μm for both materials. Several test samples with dimensions of 12 × 6 × 2 mm (from the original plate) and Ø10 × 1 mm (from the bar material) were machined out by wire-cutting for hydrogen charging experiments. The length, width and thickness directions of the rectangular-shaped pieces produced correspond to the rolling direction (RD), transverse direction (TD) and normal direction (ND) of the initial plate, respectively, and the axial direction of the discs is parallel to the extrusion direction (ED) of the original bar. Samples for hydrogenation were first immersed in an acid solution consisting of HF (10 ml), HNO₃ (45 ml) and distilled water (10 ml) for 2 min, to remove the oxide layer present on the surface that was generated during wire-cutting, and then gaseously hydrided in a Sieverts device (Advanced Materials Corporation, USA) using high-purity hydrogen (99.9%) at a pressure of 20 atm (1 atm = 101 325 Pa). Three identical thermal cycling processes were conducted to prepare the hydrided samples. For each thermal cycle, the samples were

soaked at a temperature of 723 K for 5 h, followed by furnace cooling with an approximate cooling rate of 2.2 K min^{-1}.

2.2. Microstructural characterization

The microstructure of the hydrided Zr-4 samples was characterized using optical microscopy (OM), scanning electron microscopy (SEM), electron backscattered diffraction (EBSD) and TEM. For the OM and SEM observations, Zr-4 samples were cut after hydriding, mounted in epoxy and polished according to standard metallographic techniques. These samples were further etched with a solution consisting of HF (10 ml), HNO$_3$ (100 ml) and distilled water (100 ml) for 30 s, and then observed using a Leica DMRM optical microscope under polarized light and by a JEOL JSM-6490LA scanning electron microscope operated at 20 kV. EBSD measurement of a hydrided plate sample was performed using a Zeiss Ultra Plus field-emission gun scanning electron microscope equipped with an Oxford/HKL system operating at 30 kV. Samples for EBSD analysis were prepared by mechanical grinding and further electropolishing, applying an electrolyte consisting of 95% CH$_3$OH and 5% HClO$_4$ at 30 V DC and 298 K. A step size of 0.25 μm was used for the EBSD scans and the acquired EBSD data were processed with the software packages HKL Channel5 (Oxford Diffraction, 2001) and MTEX (Hielscher & Schaeben, 2008). The interior grain structures of the hydrided Zr-4 materials were investigated using a high-resolution JEOL JEM-3000F transmission electron microscope and thin foil samples sectioned from the rolling–normal plane of a hydrided plate sample. The TEM thin foils were prepared by twin-jet electropolishing using a Struers TenuPol-5 electropolisher and an electrolyte containing 75% CH$_3$COOH and 25% HClO$_4$ at 298 K.

2.3. Bulk texture measurements

The macroscopic textures of the virgin and hydrided samples were measured using neutron diffraction at a beam wavelength (λ) calibrated to be 2.414 Å on the high-intensity powder diffractometer Wombat (Studer et al., 2006) at the Australian Nuclear Science and Technology Organisation. The tested samples were mounted on an Eulerian cradle and their corresponding diffraction images were recorded using a position-sensitive area detector. For measurement of the complete pole figure, samples were tilted (χ = 0–90°) and rotated (φ = 0–360°) in equidistant steps, typically on a 15 × 5° grid in a three-dimensional orientation sphere. Each diffraction image was divided equally into three sections and a diffraction pattern was constructed from each section. Subsequently, the resultant diffractograms were analysed to extract pole-figure data, including the diffraction peak integral intensity and pole-figure coordinates, using the software package 2DiffCalc (Garbe, 2009). Generated pole-figure data belonging to the same phase were used to determine the orientation distribution function (ODF) by adopting the MTEX algorithm (Hielscher & Schaeben, 2008). No sample symmetry was imposed to calculate the ODF in the present analysis.

2.4. Neutron diffraction pattern analysis

Representative neutron diffractograms extracted from the texture measurements were also used for a line-broadening analysis of the diffraction peak profile. The profile of all accessible peaks from the observed phases was fitted using a pseudo-Voigt function and the background was fitted assuming a linear shape. The peak parameters, including the peak position and integral intensity and breadth, were determined by this fitting. The instrumental effect on the line broadening was corrected to reveal the physical broadening of the diffraction peaks through a measurement on a stress-free and coarse-grained NIST standard LaB$_6$ powder sample. The inherent correlation of the defined physical broadening of the peak profiles with the average coherent domain size (D) and mean microstrain ($\langle\varepsilon^2\rangle^{1/2}$) of different phases in the sample can be described by the Scherrer–Wilson equation (Klug & Alexander, 1974),

$$\frac{\beta_{hkl}^2}{\tan^2\theta_{hkl}} = \frac{\lambda\beta_{hkl}}{D_{hkl}\tan\theta_{hkl}\sin\theta_{hkl}} + 16\langle\varepsilon_{hkl}^2\rangle, \qquad (1)$$

where $2\theta_{hkl}$ is the peak position and β_{hkl} is the integral breadth of the physical broadening peak profile, and D_{hkl} and $\langle\varepsilon_{hkl}^2\rangle^{1/2}$
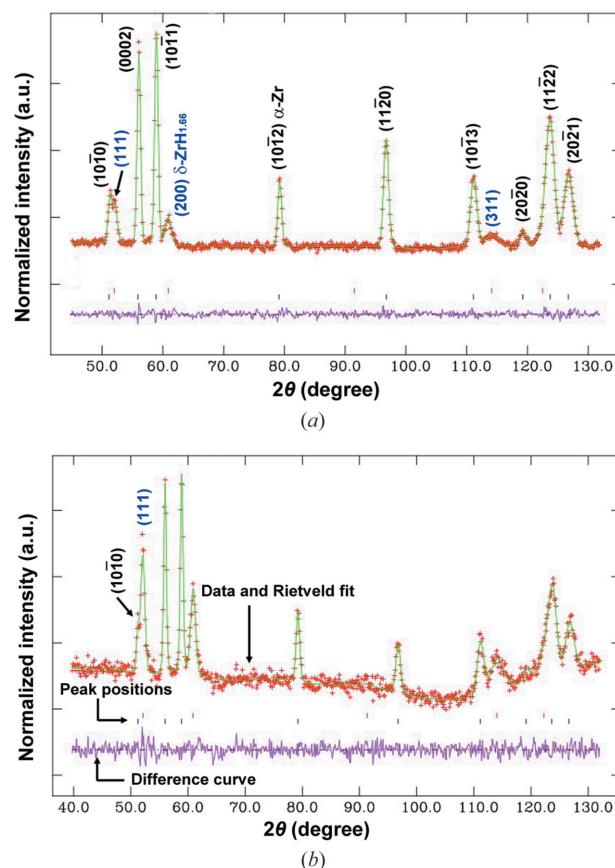

Figure 1
GSAS Rietveld refinements of typical neutron diffractograms acquired from texture measurements of the different hydrided samples: (a) the hydrided plate and (b) the hydrided bar. Diffraction peaks corresponding to α-Zr and δ-hydride are representatively indexed in (a). Each graph shows the measured data points (+ symbols), the fitted line (continuous line through the measured data points) and their difference curve.

denote the coherent domain size and mean lattice strain of the grains in the $\langle hkl \rangle$ crystallographic direction, respectively. By performing a linear least-squares fit to the plot of $\beta_{hkl}^2/\tan^2\theta_{hkl}$ versus $\lambda\beta_{hkl}/(\tan\theta_{hkl}\sin\theta_{hkl})$ for all measured peaks of the same phase in the sample, the average coherent domain size D and the microstrain $\langle\varepsilon^2\rangle^{1/2}$ can be calculated from the slope and the intercept, respectively.

Additionally, the neutron diffractograms obtained from the hydrided samples were also analysed using the Rietveld refinement technique implemented in *GSAS* (Larsen & Von Dreele, 2004) for the determination of the hydride phase fractions.

3. Results and discussion

3.1. Phase analysis

Figs. 1(*a*) and 1(*b*) show typical neutron diffraction patterns for the hydrided plate and bar samples, respectively. The diffraction peaks corresponding to hexagonal close-packed (h.c.p.) α-Zr [JCPDS (ICDD, 2005) card No. 05-0665] and f.c.c. δ-ZrH$_{1.66}$ (JCPDS card No. 34-0649) were generally identified in both hydrided samples [see the representatively indexed pattern in Fig. 1(*a*)]. The presence of δ-hydrides was unam-

biguously manifested by the detected δ-hydride diffraction peaks with relatively low intensities, including the $\delta(111)$, $\delta(200)$ and $\delta(311)$ peaks. No other hydride phases (such as γ-ZrH or ε-ZrH$_2$) were observed in this study. The diffractograms presented here were also used for the diffraction line profile analysis that will be described in §3.5. Rietveld refinement of the representative neutron diffraction patterns of the hydrided Zr-4 samples obtained at specific sample orientations was performed to quantify the hydrides formed, using *GSAS* with the generalized spherical-harmonics description for texture (Larsen & Von Dreele, 2004). The basis of this phase quantification analysis is the correlation between the weight fraction of a phase and the scale factor derived from the Rietveld analysis, which can be written as (Hill & Howard, 1987; Wang *et al.*, 2013)

$$W_p = S_p(ZMV)_p \Big/ \sum_i^n S_i(ZMV)_i, \tag{2}$$

where W_p is the weight fraction of phase p in a multiphase system with n phases, and S, Z, M and V are, respectively, the Rietveld scale factor, the number of formula units per cell, the mass of the formula unit (in atomic mass units) and the unit cell volume (in Å^3). Through this approach, the weight fractions of the δ-ZrH$_{1.66}$ phase in the hydrided plate and bar
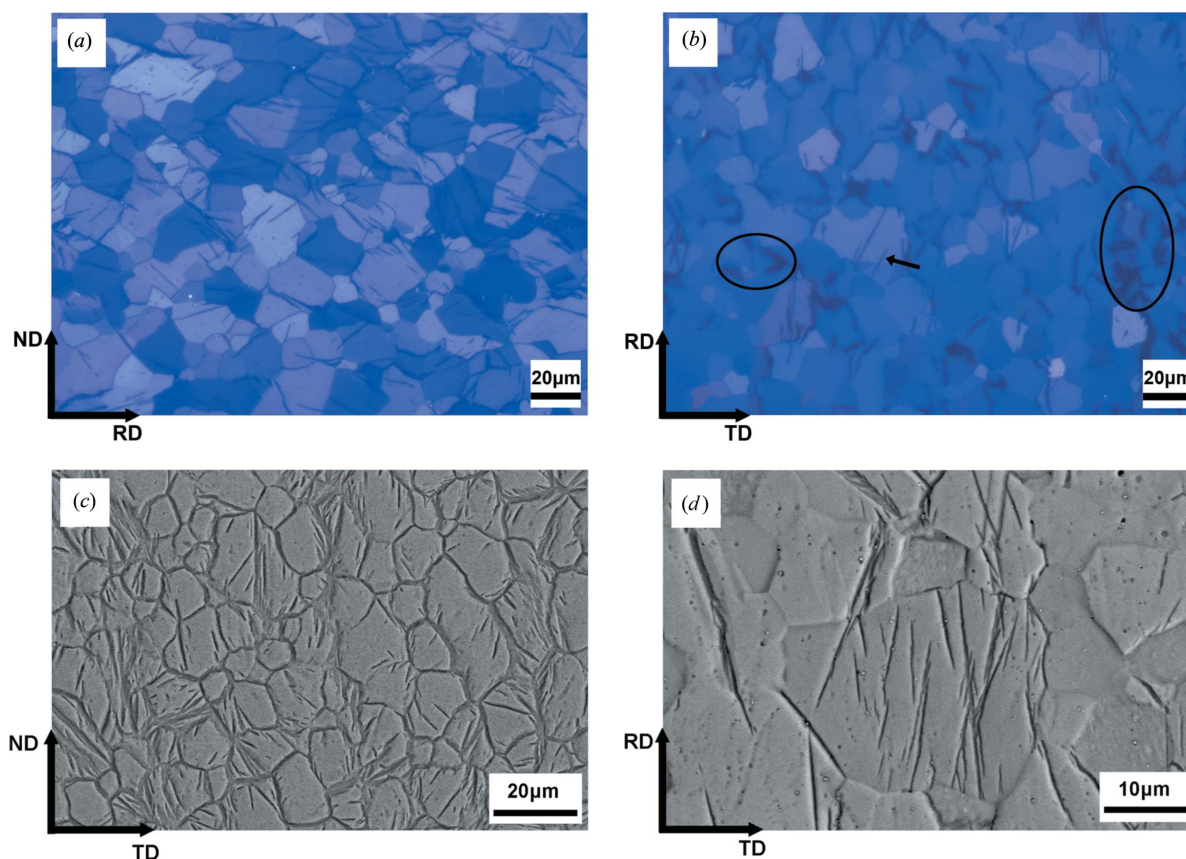

Figure 2
SEM and polarized-light micrographs of the hydrided Zr-4 plate observed on various sections: (*a*) the ND–RD section; (*b*) the RD–TD section and (*c*) the ND–TD section. (*d*) High-magnification image taken on the RD–TD section, demonstrating clear evidence of hydrides being restricted within individual α-Zr grains. The apparent transgranular hydride is indicated by a black arrowhead and some coarse hydrides are highlighted by black ellipses in (*b*). SEM images were taken in backscattered electron imaging mode. RD, TD and ND are the plate rolling, transverse and normal directions, respectively.

materials are determined to be 10 and 14 wt%, respectively, and the corresponding hydrogen contents can thus be estimated to be 1787 and 2500 wt p.p.m.

3.2. Microstructure observation

Typical microstructures of Zr-4 plate and bar materials subjected to hydrogen charging are presented in Figs. 2 and 3, respectively. Both hydrided samples exhibit characteristic microstructures, with a large number of platelet-like hydrides in the form of inter- and intragranular precipitates embedded in the α-Zr matrix. Specifically for the hydride plate, the polarized-light micrographs (Figs. 2a and 2b) taken from the ND–RD and RD–TD sections show that hydride platelets tend to align close to the RD of the plate, as the hydride prefers to form with its longitudinal direction parallel to the direction of prior sample strain (Parry & Evans, 1962; Oh et al., 2010). As apparently revealed in the plate RD–TD sectional microstructure, with some relatively coarse platelets highlighted by black ellipses (Fig. 2b), the precipitated hydride platelets demonstrate different thicknesses. This discrepancy, reflected in metallographic observations, is an indication of the actual variation in the hydride platelet thickness and/or the different spatial arrangement of hydrides. In the ND–TD section of the plate (Fig. 2c) and the cross section of the bar (Fig. 3), intergranular hydrides are predominantly precipitated and form a continuous network along the grain boundaries.

It is worth mentioning that, owing to the intrinsically brittle nature of δ-hydrides at either room or high temperature, as indicated by their extremely low fracture toughness (∼1 MPa m$^{1/2}$ at 293 K and ∼3 MPa m$^{1/2}$ at 573 K; Simpson & Cann, 1979), they may act as fracture initiators in the hydrided materials under stress-loading conditions. The microstructural configuration with the intergranular hydride network (Figs. 2c and 3) may cause significant intergranular fracture under the application of stress and thus induce serious degradation of structural integrity or even failure of the component.

In addition, a common structural feature in the two hydrided materials is that most intragranular hydrides are restricted within individual grains, with the exception of a few interlinked hydrides [indicated by a black arrowhead in Fig. 2(b)] passing through the grain boundaries. Note that the interlinked hydrides are precipitated in adjacent grains, exhibiting a similar colour in the polarized-light micrograph (Fig. 2b), which implies low misorientation. These results are consistent with the suggestion that grain-boundary misorientation is an important factor governing the development of interlinked hydride configuration (Szpunar et al., 2012). Microstructure observation on the RD–TD section at a higher magnification, as shown in Fig. 2(d), further reveals the typical hydride features that a majority of intragranular hydrides are constrained in individual α-Zr grains and transgranular hydrides seldom appear. Moreover, as obviously seen in Figs. 2(c) and 3(b), the intergranular hydrides are normally thicker than the intragranular ones, as the grain boundaries are favourable sites for hydride precipitation (Qin et al., 2011).

The volume fractions of hydrides formed in the hydrided samples were estimated from the analysis of optical or SEM micrographs taken from the etched microstructure of these samples, using the image-processing and analysis software ImageJ (http://rsbweb.nih.gov/ij/). In order to minimize measurement error, at least three low-magnification micrographs (images with a magnification of 500× were used for the current work) were taken from different locations on the samples, and the reported hydride volume fraction is the
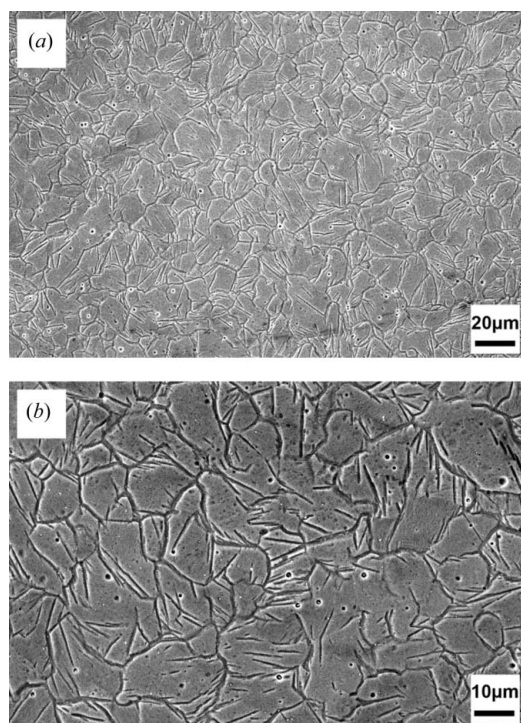

Figure 3
(a) Low- and (b) high-magnification SEM micrographs, showing typical microstructures in the cross section of the hydrided Zr-4 bar. The micrographs were taken in secondary electron imaging mode.
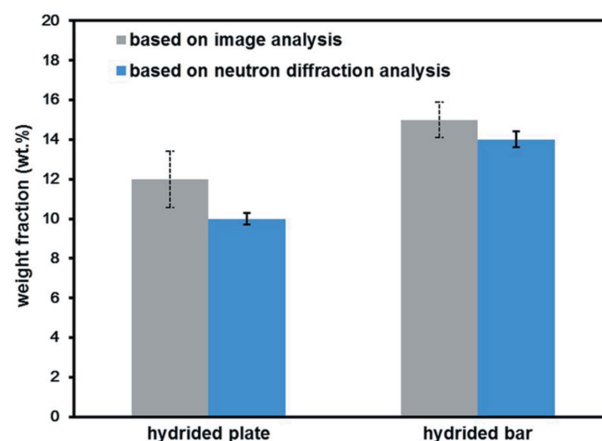

Figure 4
Quantification of hydrides in the hydrided plate and bar materials, based on image and neutron diffraction analyses. The dashed error bars in the hydride-content data obtained from SEM image analysis show the standard errors from three or more measurements, while the solid error bars represent the errors in the Rietveld phase quantification analysis which are reported by the GSAS program.

average of these measurements. Fig. 4 summarizes the hydride quantification results for the hydrided plate and bar materials based on two different approaches, *i.e.* image and neutron diffraction analyses. For a direct comparison, the hydride volume fractions (V_δ) obtained from image analysis are converted into weight fractions (W_δ) according to the following relation:

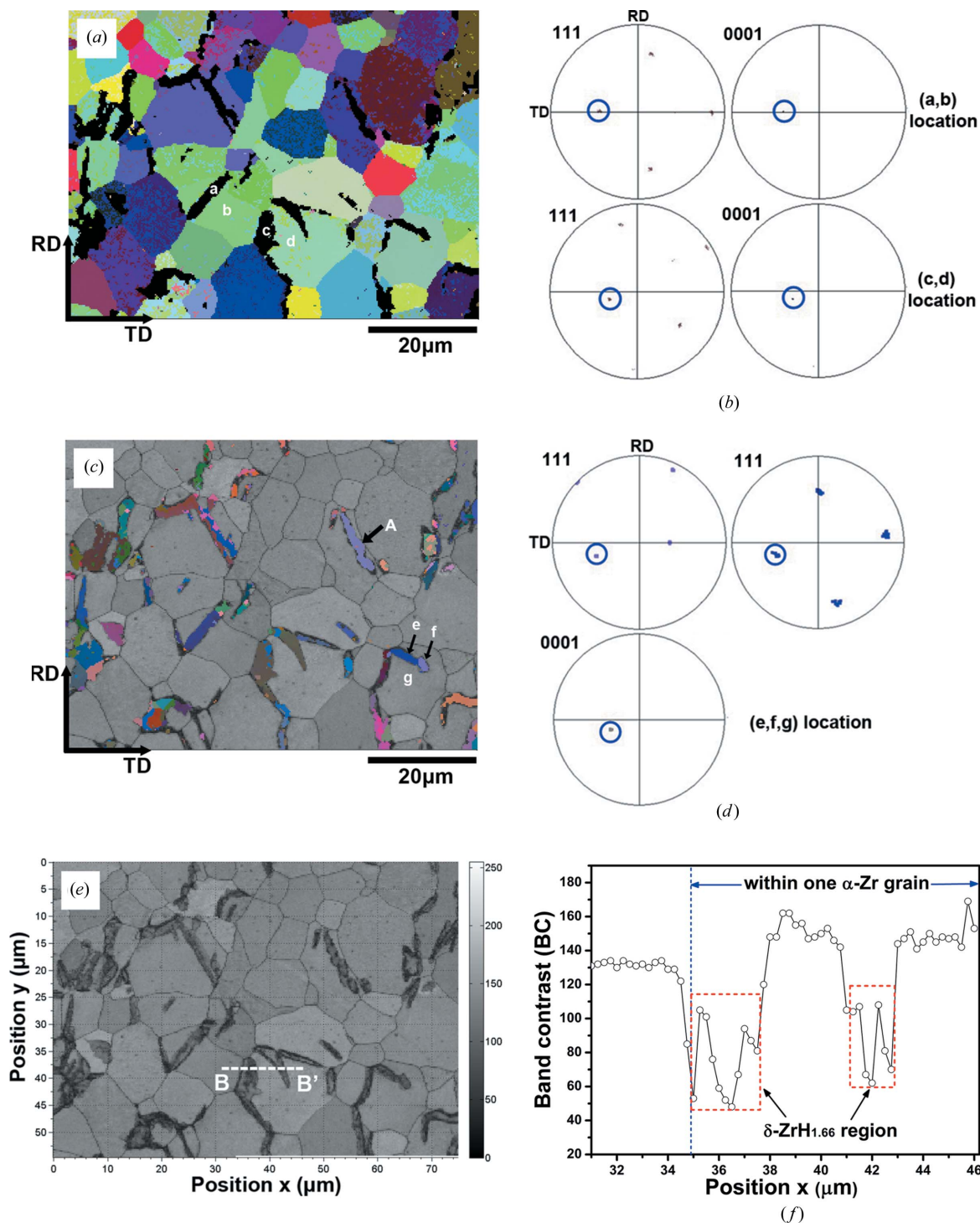$$W_\delta = \frac{\rho_\delta V_\delta}{\rho_{\alpha\text{-Zr}}(1 - V_\delta) + \rho_\delta V_\delta},$$ (3)

Figure 5
EBSD results for the hydrided Zr-4 plate. (*a*) All-Euler map in which the black regions correspond to δ-ZrH$_{1.66}$ grains. (*c*) Hydride orientation map coloured using the all-Euler colouring scheme, superimposed on the band contrast (BC) map of α-Zr grains. (*b*) and (*d*) Pole figures illustrating the orientation relationship between δ-ZrH$_{1.66}$ and α-Zr. (*e*) A BC map of the matrix and δ-hydrides. (*f*) The distribution of BC value along the line BB′ in (*e*), which crosses a region with both α-Zr and δ-hydride. The microstructure shown in (*a*) and (*c*) was reconstructed from the EBSD data using the *HKL Channel 5* software, while the reconstruction of the microstructure in (*e*) was achieved using the *MTEX* algorithm.

where ρ_δ is the density of δ-hydride at room temperature ($\sim$5.65 g cm^{-3}) and $\rho_{\alpha\text{-Zr}}$ is the density of α-Zr at room temperature ($\sim$6.51 g cm^{-3}). In general, the proportion of hydride precipitates estimated from metallographic observation is quite close to that extracted from the neutron diffraction evaluation. This comparison demonstrates that the observation of local structure in hydrided samples by microscopy is in good agreement with the overall (or average) structural characteristics of bulk samples obtained using neutron diffraction.

The α-Zr and δ-hydride phases present in the hydrided Zr-4 sample were also identified by indexing the Kikuchi patterns using EBSD. An all-Euler map taken from the RD–TD section of hydrided Zr-4 is displayed in Fig. 5(a), where the α-Zr grains are mapped with a different colour based on their crystal orientation represented by Euler angles, whereas the δ-hydride grains are marked in black. The characteristic inter- and intragranular hydrides are also observed, and the constrained growth of intragranular hydrides by the surrounding α-Zr grain boundaries with large misorientations is confirmed. The hydride crystallographic orientations with respect to the α-Zr matrix are determined using pole figures with the EBSD technique. At all locations (Fig. 5a), the inter- and intragranular hydrides were found to follow a $\delta(111)//\alpha(0001)$ orientation relationship (OR) with the surrounding α-Zr grains, as illustrated representatively in Fig. 5(b). This OR result is in line with previous studies using TEM (Perovic et al., 1983; Neogy et al., 2003) and, because of the statistically more complete observations of the EBSD map (Fig. 5a), it reliably reveals the common OR between δ-hydride and the matrix in a hydrided Zr-4 alloy. Fig. 5(c) shows the hydride orientation map, coloured using the all-Euler colouring scheme and superimposed on the band-contrast (BC) map of α-Zr grains. Most hydride platelets, including the longest one observed in Fig. 5(c) which has a length of $\sim$10 μm (denoted by arrow A), exhibit a single orientation, and such orientation behaviour was also reported for δ-hydride platelets in Zr-2.5Nb alloy by EBSD measurements (Mani Krishna et al., 2011). Although the majority of hydride platelets have a single orientation, individual platelets having different orientations were occasionally observed. As indicated in Fig. 5(c), a long hydride plate was found to have two short strings (marked by arrows e and f), demonstrating its clearly distinct orientation. According to the Euler angles of the hydride strings from EBSD data, the misorientation angle between them was calculated to be $\sim$60° with a rotation axis of $\langle 111 \rangle$ and, interestingly, these two hydride strings maintain the $\delta(111)//\alpha(0001)$ correlation with the surrounding α-Zr grains according to the pole figure analyses illustrated in Fig. 5(d).

The precipitation of hydride strings in the same α-Zr grains but with varied orientation, which is analogous to the formation of martensite variants in ferrous alloys, promotes the self-accommodation of strain arising from the large volume expansion of δ-hydrides (17.2%; Carpenter, 1973) relative to the α-Zr matrix. Our EBSD results (Figs. 5a and 5c) reveal that, in most cases, inter- and intragranular hydride platelets characterized by a single orientation in individual platelets are

observed, as the dilatational strain associated with the formation of δ-hydrides could be favourably accommodated by the grain boundary itself or by elastic distortion/plastic deformation (i.e. the generation of misfit dislocations) in the α-Zr and δ-hydride grains involved (Bai, Prioul & François, 1994; Lufrano et al., 1998; Mani Krishna et al., 2006). In addition to the observed single orientation of most individual δ-ZrH$_{1.66}$ platelets, the BC map of Fig. 5(e) implies another interesting microstructural feature of the hydrided plate, i.e. the BC of δ-hydride (reflected by the corresponding BC value) is generally weaker than that of α-Zr. It should be mentioned that the BC depends on the sample surface quality and the measurement conditions, as well as on the microstructural characteristics (lattice distortion or dislocation density) (Petrov et al., 2007). As the hydride demonstrates a commonly weaker BC than α-Zr in the same EBSD measurement (Fig. 5e), it is reasonable to deduce that a relatively high lattice distortion (strain or dislocation) may exist in the δ-hydride phase. Furthermore, Fig. 5(f) shows the distribution of the BC values along the white dashed line (BB'), which crosses a region with both α-Zr and δ-hydride (Fig. 5e). To exclude the subtle influence of grain orientation on BC, the distribution of
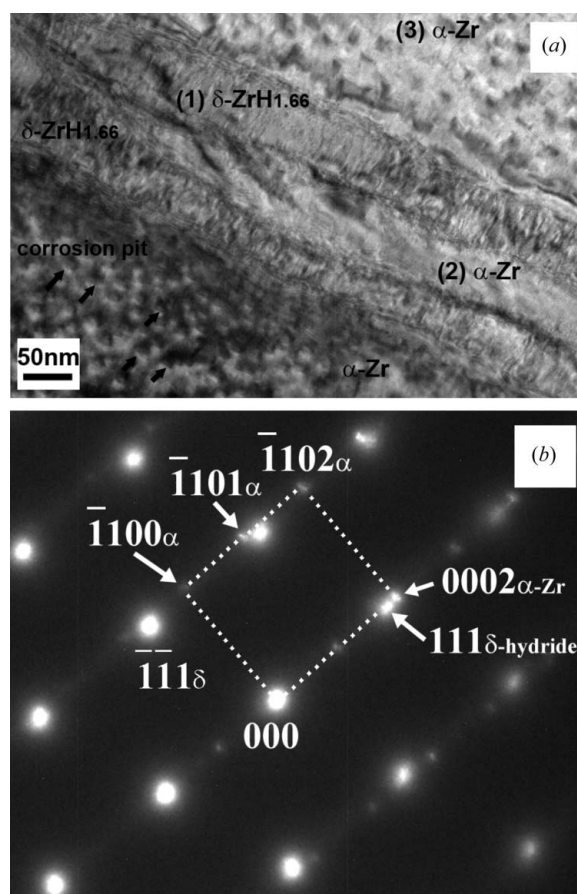

Figure 6
(a) A bright-field TEM image and (b) the corresponding composite SAED pattern, showing the δ-ZrH$_{1.66}$ platelets formed in the α-Zr matrix of the hydrided plate. Note that some corrosion pits appear in the α-Zr matrix, as indicated by black arrowheads in (a); these were probably generated in the twin-jet thinning process for TEM sample preparation.

the BC parameter in different phases was fairly compared within one α-Zr grain region (Fig. 5f). This comparison consistently suggests a generally stronger BC for α-Zr than for δ-hydride. Also, a relatively low BC value was detected in a narrow α-Zr region ($<0.25\ \mu m$) near the hydride/matrix interface.

Fig. 6(a) provides a bright-field TEM image recorded from the hydrided plate sample, showing an example of the subtle microscopic structure of a δ-hydride platelet with two developed branches. A selected-area electron diffraction (SAED) pattern taken from the hydride and matrix in Fig. 6(a) is presented in Fig. 6(b), from which the OR between the hydride and the α-Zr matrix can be identified as $\delta(111)//\alpha(0001)$ and $\delta[1\bar{1}0]//\alpha[11\bar{2}0]$. This hydride–matrix OR is in agreement with the finding from the present EBSD observations (Figs. 5b and 5d) and was also reported in previous studies on hydrided Zircaloy-2 (Bradbrook et al., 1972; Une & Ishimoto, 2006, 2009) and Zr-2.5Nb (Mani Krishna et al., 2011) alloys. The prevalence of this crystallographic relation, as shown schematically in Fig. 7 (Li et al., 1999), is essentially due to the preferred lattice matching of the $(0001)_{\alpha\text{-Zr}}$ and $\{111\}_{\delta\text{-ZrH1.66}}$ atomic planes involved, which could contribute to minimizing the strain energy for the α-Zr (h.c.p.) $\rightarrow$ δ-ZrH$_{1.66}$ (f.c.c.) phase transformation (Carpenter, 1973; Kiran Kumar et al., 2010).

3.3. Texture evaluation

In order to gain an insight into the characteristics and origin of hydride texture, it is essential to perform a texture analysis on both the hydride precipitate and the matrix phases in different textured Zr-4 materials. Figs. 8(a) and 9(a) show the experimental $\{0002\}$ and $\{10\bar{1}0\}$ α-Zr pole figures for the virgin Zr-4 plate and bar materials, respectively, and Figs. 8(b) and 9(b) display the experimental $\{111\}$ and $\{200\}$ pole figures of δ-ZrH$_{1.66}$ formed in the two corresponding hydrided materials.
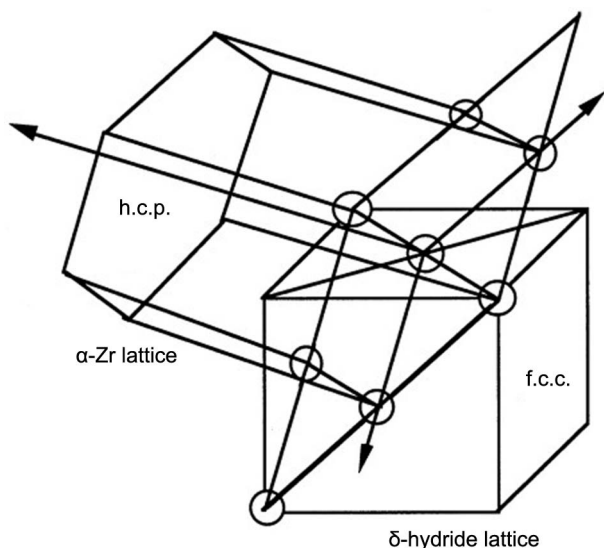

Figure 7
Schematic drawing showing the orientation relationship between α-Zr and δ-ZrH$_{1.66}$ (Li et al., 1999).

Table 2
Quantitative information for the measured texture of different phases in the virgin and hydrided Zr-4 plate and bar materials.

Phases	Pole figure maximum (m.r.d.)	ODF maximum (m.r.d.)	Texture index
α-Zr in the virgin plate	4.5	5.1	2.1
δ-ZrH$_{1.66}$ in the hydrided plate	1.7	2.2	1.2
α-Zr in the virgin bar	3.5	3.8	1.9
δ-ZrH$_{1.66}$ in the hydrided bar	1.6	2.1	1.1

Pole figures presented here were recalculated from the experimental ODF determined by neutron diffraction. The measured texture for both phases is expected to have high reliability, as 1512 different sample orientations were involved in the present full texture measurements. Table 2 summarizes some quantitative details of the texture (pole figure maxima, ODF maxima and texture index). As clearly indicated by the pole figures in Figs. 8(a) and 9(a), the initial plate and bar materials had distinctly different crystallographic textures (especially the basal textures), which essentially result from their different thermomechanical treatments. For the virgin plate, the $\{0002\}$ basal planes present the double pole maxima lying on the ND–TD plane of the plate at angles of around $\pm 30^\circ$ to the ND, and the prismatic $\{10\bar{1}0\}$ planes show a strong pole along the RD (Fig. 8a) (Wang et al., 2013). The α-Zr texture for the plate is similar to that observed in cold-rolled zirconium sheet using high-energy X-ray diffraction (Ischia et al., 2005), and this reported result is in good agreement with the previous finding of Carr et al. (2004) on the same material but measured by time-of-flight neutron diffraction, indicating the reliability of our neutron texture measurements and data processing. In contrast with the plate material, the $\{0002\}$ basal planes and the prismatic poles (i.e. the $\langle 10\bar{1}0\rangle$ crystal directions) of α-Zr grains in the starting bar material are predominantly aligned parallel to the ED of the bar (Fig. 9a), demonstrating the typical features of fibre texture. Besides the evident difference in the shape of the α-Zr pole figures, the intensity of the α-Zr texture for the bar material is slightly weaker than that for the plate, as revealed by the quantitative parameters describing the sharpness of the texture listed in Table 2 (for example, the texture index for the bar material is 1.9, while for the plate it is 2.1).

For the measured texture of the δ-ZrH$_{1.66}$ phase in the two hydrided materials, some relevant characteristics can be captured by the present observations (Figs. 8b and 9b) and through comparison with previous studies (Santisteban et al., 2010; Vicente Alvarez et al., 2011). The δ-hydrides in the hydrided samples both present a weak texture, manifested by the relatively low values of the texture parameters listed in Table 2. For example, the pole maximum is 1.7 multiples of the random distribution (m.r.d.) and the texture index is 1.2 for the experimental texture of δ-hydride in the hydrided plate, slightly larger than the corresponding values for the texture of δ-hydride in the hydrided bar (pole maximum 1.6 m.r.d. and texture index 1.1). Vicente Alvarez et al. (2011) performed a texture analysis of a hydride blister in a Zr-2.5Nb tube with an

apparently sharper α-Zr texture (texture index ∼7) compared with that for the two Zr-4 materials in this work, using synchrotron X-ray diffraction, implying a weak δ-hydride texture with a texture index of ∼2.3. This result, together with the present findings on δ-hydride texture (Figs. 8b and 9b), suggests that δ-hydrides precipitated in various zirconium alloys generally exhibit a weak texture with an intensity appreciably lower than that of the α-Zr matrix. On the basis of a study by Vicente Alvarez et al. (2011), the marked decrease in intensity of the δ-hydride texture is related to the cubic symmetry of the δ-hydride phase and the OR existing between α-Zr and δ-hydride, which involves different precipitation variants. Moreover, Santisteban et al. (2010) reported the δ-hydride texture obtained from a warm-rolled Zr-4 plate containing only 180 wt p.p.m. of hydrogen by synchrotron

X-ray diffraction, very similar to that measured from the hydrided plate in our experiment (Fig. 8b) with an approximate hydrogen content of 1787 wt p.p.m.. They also identified the weak texture characteristics of δ-hydrides with a pole maximum of 2.3 m.r.d. and a texture index of 1.22.

These observations regarding the δ-hydride texture from the two Zr-4 plate materials referred to above with the expected similar matrix texture reveal that the δ-hydride texture is basically independent of the hydrogen content, which was also verified by the previous investigation on a hydride blister in Zr-2.5Nb (Vicente Alvarez et al., 2011).

The most interesting observation of the δ-hydride texture is that the {111} pole figure of δ-hydrides almost resembles the features of the {0002} α-Zr pole figure for the corresponding virgin material in terms of the dominant shape and locations of the local pole maxima (Figs. 8a, 8b, 9a and 9b). This pole figure
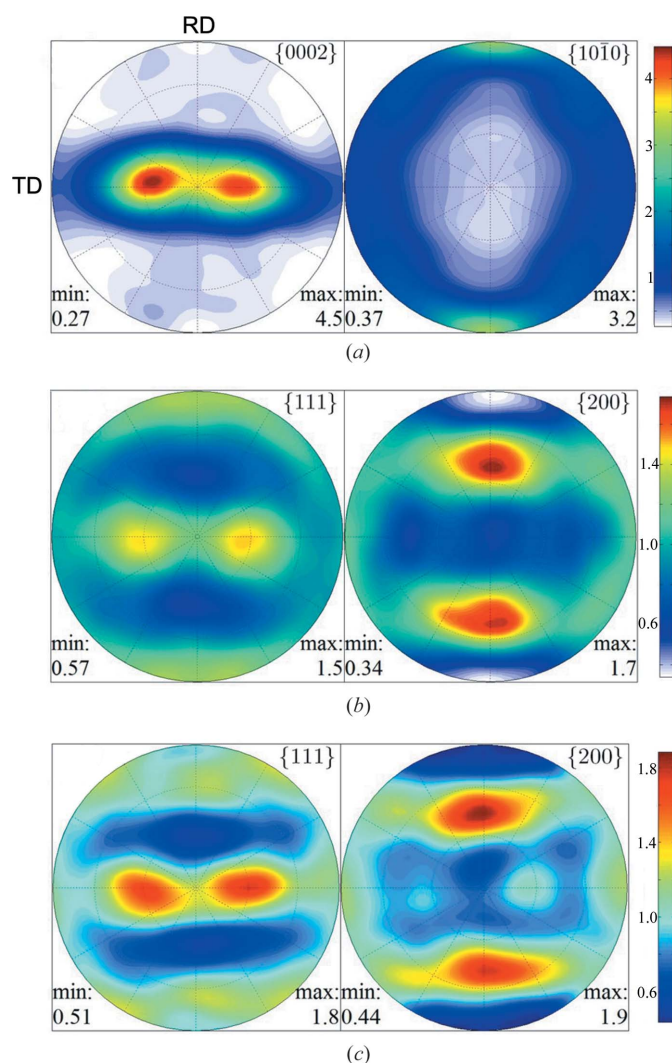

Figure 8
Experimental pole figures of different phases determined by neutron diffraction: (a) the α-Zr phase of the virgin Zr-4 plate (Wang et al., 2013) and (b) the δ-hydride phase precipitated in the plate. (c) Predicted pole figures of the δ-hydrides formed in the plate, obtained by applying the δ(111)//α(0001) and δ[1$\bar{1}$0]//α[11$\bar{2}$0] orientation relationship to the ODF of the α-Zr phase in the plate. The plate-rolling direction (RD) and transverse direction (TD) are indicated, and the normal direction (ND) is in the centre.
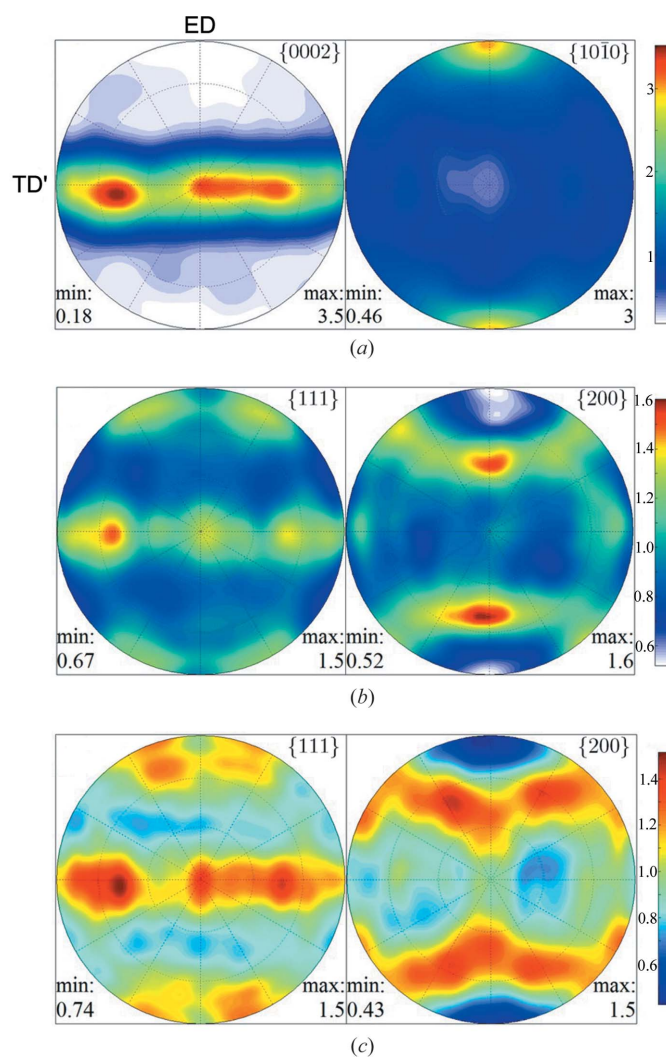

Figure 9
Pole figures of different phases determined by neutron diffraction: (a) the α-Zr phase of the virgin Zr-4 bar and (b) the δ-hydride phase precipitated in the bar. (c) Predicted pole figures of the δ-hydrides formed in the bar, obtained from the experimental ODF of the α-Zr phase in the extruded bar and the δ(111)//α(0001) and δ[1$\bar{1}$0]//α[11$\bar{2}$0] orientation relationship. The extrusion direction (ED) and tangential direction (TD′) of the bar material are indicated, and the radial direction is in the centre.

Table 3
Microstructural parameters of the hydrided Zr-4 plate and bar samples as determined by neutron diffraction line profile analysis.

Parameters	α-Zr in the hydrided plate	δ-ZrH$_{1.66}$ in the hydrided plate	α-Zr in the hydrided bar	δ-ZrH$_{1.66}$ in the hydrided bar
D (nm)	88	17	61	21
$\langle \varepsilon^2 \rangle^{1/2}$ (%)	0.057	0.25	0.087	0.23
ρ ($\times 10^{14}$ m^{-2})	0.44	15	0.96	11.6

result can be properly explained by considering the OR between the δ-hydride and the α-Zr matrix as suggested by EBSD and TEM measurements (Figs. 5*b*, 5*d* and 6*b*). Following the procedure described by Santisteban *et al.* (2010) and Vicente Alvarez *et al.* (2011), the theoretical {111} and {200} pole figures of δ-hydrides in the hydrided plate and bar materials [as illustrated in Figs. 8(*c*) and 9(*c*), respectively] were calculated from the α-Zr ODF of the relevant virgin Zr-4, by applying the common orientation relation between α-Zr and δ-hydride reported in the present work, *i.e.* $\delta(111)//$ $\alpha(0001)$ and $\delta[1\bar{1}0]//\alpha[11\bar{2}0]$. The α-Zr ODF of the starting Zr-4, not shown here, was estimated from the pole figure data from the current neutron diffraction experiments using *MTEX*. The measured and simulated δ-hydride pole figures in the two cases generally exhibit good agreement in the primary pole intensity and submaxima locations, as indicated in Figs. 8(*b*), 8(*c*), 9(*b*) and 9(*c*). These findings suggest that δ-hydride commonly obeys the $\delta(111)//\alpha(0001)$ and $\delta[1\bar{1}0]//$ $\alpha[11\bar{2}0]$ OR with the α-Zr matrix of Zr-4 under the present hydriding conditions. In particular, the texture results in Figs. 9(*b*) and 9(*c*) prove that this OR is valid in the case of the hydrided bar material, although direct measurement of the OR for hydride precipitation in this material is not performed in this work. Overall, the aforementioned analysis regarding the macroscopic texture for both phases reveals that the δ-hydride precipitates display a weak macroscopic texture which is determined by the α-Zr matrix, and this dependence essentially originates from the observed predominant orientation correlation between α-Zr and δ-hydride {*i.e.* $\delta(111)//$ $\alpha(0001)$ and $\delta[1\bar{1}0]//\alpha[11\bar{2}0]$}.

3.4. Local misorientation distribution

Fig. 10(*a*) displays a local misorientation map for the hydrided Zr-4 plate sample. This map is constructed using the kernel average misorientation approach, in which each pixel in the map is coloured as a function of the average misorientation between the given pixel and all of its neighbours. Misorientation greater than 5° is excluded for this map construction. If we also consider the corresponding EBSD phase map (Fig. 5*a*), it is obvious that the hydrides generally exhibit a higher misorientation, and the specific intragranular misorientation profiles for α-Zr and δ-hydride shown in Fig. 10(*b*) also verify this point. The larger misorientation developed in the hydrides is probably due to the accumulation of considerable plastic strain and the attendant generation of misfit dislocations in the hydrides (Bai, Ji *et al.*, 1994; Mani Krishna *et al.*, 2011), which could effectively accommodate the

substantial dilatational misfit strain associated with the α-Zr (h.c.p.) $\rightarrow$ δ-ZrH$_{1.66}$ (f.c.c.) transformation.

3.5. Dislocation density estimation

The observed general characteristics of the hydrides, in terms of low BC (Fig. 5*e*) and high intragranular misorientation (Fig. 10), are rationalized by neutron diffraction line profile analysis on the hydrided Zr-4 materials described in this section, which attempts to quantify the dislocation densities in both δ-hydride and α-Zr matrix phases. Table 3 summarizes the quantitative microstructural parameters of the
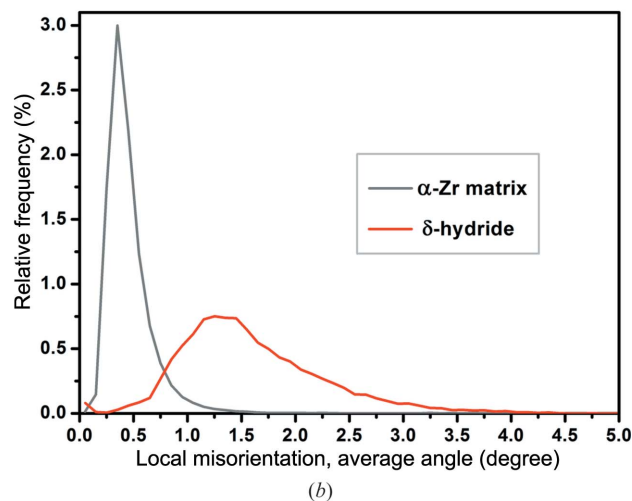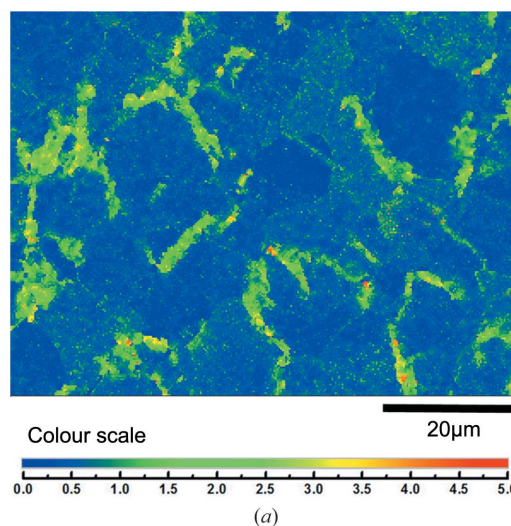

Figure 10
(*a*) A local misorientation map of the hydrided Zr-4 plate. (*b*) The average intragranular misorientation distribution in the α-Zr matrix and δ-hydride phases.

different phases in the hydrided materials (plate and bar) obtained from line profile analysis of the measured neutron diffractograms displayed in Fig. 1. The results show that, for both hydrided materials, the average coherent domain size (D) of δ-hydride ($\sim$20 nm) is much smaller than that of α-Zr ($\sim$80 nm). For the diffraction peak profile analysis, the determined coherent domain size corresponds to subgrains

and dislocation cells (Ungár *et al.*, 2005). The fine hydride platelets with a thickness of $\sim$50 nm, as seen in Fig. 6(*a*), are obviously responsible for the low D value of the hydride. In contrast, the calculated mean lattice microstrain ($\langle\varepsilon^2\rangle^{1/2}$) of the δ-hydride is significantly larger than that of the α-Zr matrix of the hydrided materials, possessing a value approximately 2.6–4.4 times that of α-Zr (Table 3). The average dislocation
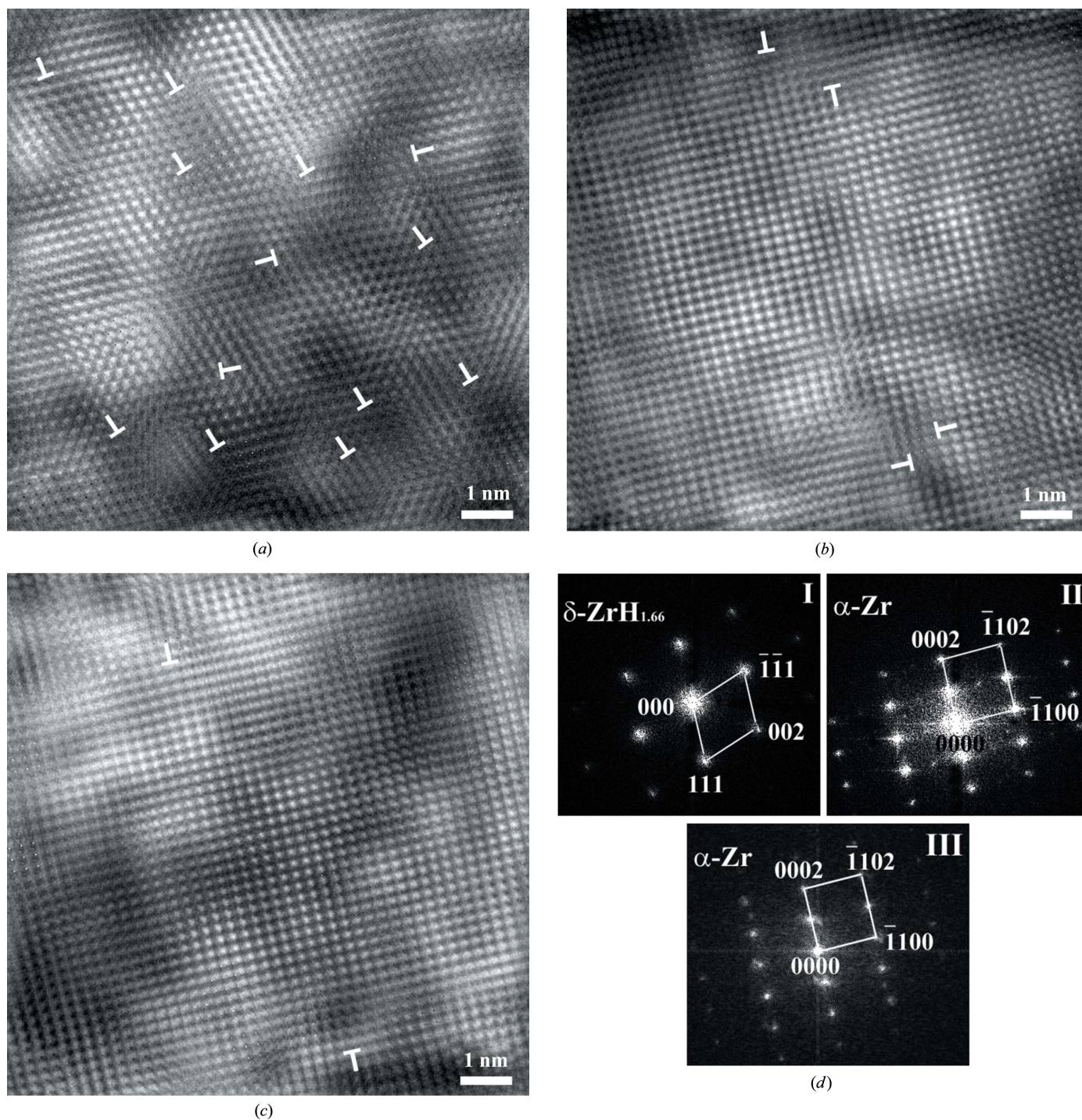

Figure 11
Typical Fourier-filtered HRTEM images of the hydrided plate sample, showing the local dislocation distributions in (*a*) the δ-hydride grain, (*b*) an α-Zr grain far away from the α/δ interface and (*c*) an α-Zr grain near the α/δ interface. Dislocation cores are indicated using 'T' symbols. Note that the approximate imaging locations of the original HRTEM images shown in (*a*), (*b*) and (*c*) are marked in Fig. 6(*a*) as (1), (2) and (3), respectively. (*d*) Three Fourier-transformed electron diffraction patterns, I, II and III, obtained from the corresponding HRTEM images of (*a*), (*b*) and (*c*), respectively.

density ρ in the different phases of the hydrided materials, which correlates with the determined average coherent domain size and mean microstrain, can be estimated *via* the relationship (Williamson & Smallman, 1956; Smallman & Westmacott, 1957; Zhao *et al.*, 2004)

$$\rho = \frac{2(3)^{1/2}\langle \varepsilon^2 \rangle^{1/2}}{Db}, \tag{4}$$

where b is the magnitude of the Burgers vector of the dislocations (b = 0.3378 nm for δ-hydride and 0.5147 nm for α-Zr). The calculated ρ values of the δ-hydride and α-Zr phases in the hydrided materials are also listed in Table 3. In the case of the hydrided plate, it is found that the calculated ρ in δ-hydride (15×10^{14} m^{-2}) is around an order of magnitude higher than that in α-Zr (0.44×10^{14} m^{-2}). A similar situation is also observed for the hydrided bar material, with the average dislocation densities in the δ-hydride and α-Zr phases estimated to be 11.6×10^{14} and 0.96×10^{14} m^{-2}, respectively. Note that the value of the average dislocation density evaluated from the neutron diffraction line profile analysis is usually only semiquantitative. However, comparison of the dislocation densities of the δ-hydride and α-Zr phases in the same hydrided material is valid as they are measured and analysed in a consistent way (Wang *et al.*, 2009).

A complementary HRTEM analysis on the hydrided Zr-4 plate sample was further conducted to reveal the local distribution of dislocations in the δ-hydride and α-Zr phases. A typical Fourier-filtered HRTEM image from a hydride platelet in the hydrided plate sample is provided in Fig. 11(a), showing a significant accumulation of dislocations. By contrast, examples of the α-Zr grains in the hydrided plate containing only a few dislocations are shown in Figs. 11(b) and 11(c). The rough imaging locations of the original HRTEM images of Figs. 11(a), 11(b) and 11(c) are marked in Fig. 6(a) as (1), (2) and (3), respectively. Fig. 11(d) illustrates the indexed electron diffraction patterns acquired from the Fourier transform of the corresponding HRTEM images, affirming that the region analysed by HRTEM corresponds to a single-constitution phase (δ-ZrH$_{1.66}$ or α-Zr). As demonstrated representatively in Figs. 11(a)–11(c), extensive HRTEM investigations over a large area of the hydrided plate sample suggest that the dislocation density in the hydride grains is noticeably higher than that in the α-Zr grains. Also, no twinning or stacking faults were found in the δ-hydride and α-Zr grains. The combination of these observations with neutron diffraction line profile analysis provides solid evidence to support the observation that misfit strains accompanied by hydride transformation are predominantly accommodated by the generation of a significant number of dislocations inside the hydrides, contributing to the development of a large misorientation in the hydrides (Fig. 10). It is thus reasonable to deduce that, besides the intrinsically brittle characteristics of hydrides, the accumulation of dislocations may be another important factor leading to their negligible plasticity at room temperature (Simpson & Cann, 1979; Puls, 1991; Bai, Prioul & François, 1994; Kerr *et al.*, 2008). In addition, Figs. 11(b) and 11(c) show HRTEM images taken from α-Zr grains close to

and far away from the α-Zr/δ-hydride interface, respectively. On the basis of this observation, it seems that more dislocations tend to be generated in the matrix near the α/δ interface than far away from the interface, which is a common phenomenon as noted in several HRTEM observations. However, this result is not conclusive, due both to the non-obvious implication of the dislocation distributions in the regions far away from and near the α/δ interface from Figs. 11(b) and 11(c) and to the lack of statistical HRTEM analyses.

4. Conclusions

In this work, the microstructure characteristics and crystallographic textures of various hydrided Zr-4 materials (hot-rolled and annealed plate, and hot-extruded and annealed round bar) containing high concentrations of hydrogen (~2000 wt p.p.m.) have been investigated in detail by neutron diffraction and microscopy. In particular, neutron diffraction line profile analysis and HRTEM observations on the hydrided samples were performed to reveal the dislocation density distributions in both hydride and matrix phases. The principal conclusions are summarized as follows:

(1) Both intra- and intergranular platelet-like precipitates (identified as δ-ZrH$_{1.66}$) are observed. Most intragranular hydrides are restricted within individual α-Zr grains, and the intergranular ones tend to form a continuous network along grain boundaries in the present high hydrogen content condition.

(2) The δ-hydride generally presents a weak texture that is dependent on that of the α-Zr matrix. This dependence essentially originates from the common $\delta(111)//\alpha(0001)$ and $\delta[1\bar{1}0]//\alpha[11\bar{2}0]$ OR that exists between the δ-hydride and the α-Zr matrix.

(3) The dislocation density in the δ-hydride is notably higher than that in the α-Zr matrix. On the basis of neutron diffraction line profile analysis, the average dislocation density in the hydride was evaluated to be around one order of magnitude higher than that in the matrix. The generation of a significant number of misfit dislocations in the hydrides is induced for the accommodation of the large misfit strains associated with hydride precipitation in the Zr-4 matrix.

References

Bai, J. B., Ji, N., Gilbon, D., Prioul, C. & François, D. (1994). *Metall. Mater. Trans. A*, **25**, 1199–1208.

Bai, J. B., Prioul, C. & François, D. (1994). *Metall. Mater. Trans. A*, **25**, 1185–1197.

Bradbrook, J. S., Lorimer, G. W. & Ridley, N. (1972). *J. Nucl. Mater.* **42**, 142–160.

Carpenter, G. J. C. (1973). *J. Nucl. Mater.* **48**, 264–266.

Carr, D. G., Ripley, M. I., Holden, T. M., Brown, D. W. & Vogel, S. C. (2004). *Acta Mater.* **52**, 4083–4091.

Colas, K. B., Motta, A. T., Almer, J. D., Daymond, M. R., Kerr, M., Banchik, A. D., Vizcaino, P. & Santisteban, J. R. (2010). *Acta Mater.* **58**, 6575–6583.

Dutton, R., Nuttall, K., Puls, M. P. & Simpson, L. A. (1977). *Metall. Mater. Trans. A*, **8**, 1553–1562.

Garbe, U. (2009). *J. Appl. Cryst.* **42**, 730–733.

Hielscher, R. & Schaeben, H. (2008). *J. Appl. Cryst.* **41**, 1024–1037.

Hill, R. J. & Howard, C. J. (1987). *J. Appl. Cryst.* **20**, 467–474.

ICDD (2005). PDF-2. International Centre for Diffraction Data, Newtown Square, Pennsylvania, USA. http://www.icdd.com.

Ischia, G., Wenk, H.-R., Lutterotti, L. & Berberich, F. (2005). *J. Appl. Cryst.* **38**, 377–380.

Kearns, J. J. (1967). *J. Nucl. Mater.* **22**, 292–303.

Kerr, M., Daymond, M. R., Holt, R. A. & Almer, J. D. (2008). *J. Nucl. Mater.* **380**, 70–75.

Kiran Kumar, N. A. P., Szpunar, J. A. & He, Z. (2010). *J. Nucl. Mater.* **403**, 101–107.

Klug, H. P. & Alexander, L. E. (1974). *X-ray Diffraction Procedures for Polycrystalline and Amorphous Materials*. New York: Wiley-VCH.

Larsen, A. C. & Von Dreele, R. B. (2004). *GSAS*. Report LAUR 86-748. Los Alamos National Laboratory, New Mexico, USA.

Li, H. J., Dunne, D. & Kennon, N. (1999). *Mater. Sci. Eng. A*, **273–275**, 517–523.

Lufrano, J., Sofronis, P. & Birnbaum, H. K. (1998). *J. Mech. Phys. Solids*, **46**, 1497–1520.

Mani Krishna, K. V., Sain, A., Samajdar, I., Dey, G. K., Srivastava, D., Neogy, S., Tewari, R. & Banerjee, S. (2006). *Acta Mater.* **54**, 4665–4675.

Mani Krishna, K. V., Srivastava, D., Dey, G. K., Hiwarkar, V., Samajdar, I. & Banerjee, S. (2011). *J. Nucl. Mater.* **414**, 270–275.

Nath, B., Lorimer, G. W. & Ridley, N. (1975). *J. Nucl. Mater.* **58**, 153–162.

Neogy, S., Srivastava, D., Tewari, R., Singh, R. N., Dey, G. K. & Banerjee, S. (2003). *J. Nucl. Mater.* **322**, 195–203.

Oh, S., Jang, C., Kim, J. H. & Jeong, Y. H. (2010). *Mater. Sci. Eng. A*, **527**, 1306–1313.

Oxford Diffraction (2001). *HKL Channel5*. Oxford Diffraction Ltd, Abingdon, England.

Parry, G. W. & Evans, W. (1962). Report AECL-1707. Atomic Energy of Canada Limited, Chalk River, Ontario, Canada.

Perovic, V., Weatherly, G. C. & Simpson, C. J. (1983). *Acta Metall.* **31**, 1381–1391.

Petrov, R., Kestens, L., Wasilkowska, A. & Houbaert, Y. (2007). *Mater. Sci. Eng. A*, **447**, 285–297.

Puls, M. P. (1984). *Acta Metall.* **32**, 1259–1269.

Puls, M. P. (1990). *Metall. Mater. Trans. A*, **21**, 2905–2917.

Puls, M. P. (1991). *Metall. Trans. A*, **22**, 2327–2337.

Qin, W., Kiran Kumar, N. A. P., Szpunar, J. A. & Kozinski, J. (2011). *Acta Mater.* **59**, 7010–7021.

Qin, W., Szpunar, J. A. & Kozinski, J. (2012). *Acta Mater.* **60**, 4845–4855.

Santisteban, J. R., Vicente-Alvarez, M. A., Vizcaíno, P., Banchik, A. D. & Almer, J. D. (2010). *Acta Mater.* **58**, 6609–6618.

Shi, S. Q., Shek, G. K. & Puls, M. P. (1995). *J. Nucl. Mater.* **218**, 189–201.

Simpson, L. A. & Cann, C. D. (1979). *J. Nucl. Mater.* **87**, 303–316.

Smallman, R. E. & Westmacott, K. H. (1957). *Philos. Mag.* **2**, 669–683.

Studer, A. J., Hagen, M. E. & Noakes, T. J. (2006). *Physica B*, **385–386**, 1013–1015.

Szpunar, J. A., Qin, W., Li, H. & Kiran Kumar, N. A. P. (2012). *J. Nucl. Mater.* **427**, 343–349.

Une, K. & Ishimoto, S. (2006). *J. Nucl. Mater.* **357**, 147–155.

Une, K. & Ishimoto, S. (2009). *J. Nucl. Mater.* **389**, 436–442.

Ungár, T., Tichy, G., Gubicza, J. & Hellmig, R. J. (2005). *Powder Diffr.* **20**, 366–375.

Vicente Alvarez, M. A., Santisteban, J. R., Domizzi, G. & Almer, J. (2011). *Acta Mater.* **59**, 2210–2220.

Vicente Alvarez, M. A., Santisteban, J. R., Vizcaino, P., Flores, A. V., Banchik, A. D. & Almer, J. (2012). *Acta Mater.* **60**, 6892–6906.

Wang, Z. Y., Garbe, U., Li, H. J., Harrison, R. P., Toppler, K., Studer, A. J., Palmer, T. & Planchenault, G. (2013). *J. Nucl. Mater.* **436**, 84–92.

Wang, Z. Y., Garbe, U., Li, H. J., Studer, A. J., Harrison, R. P., Callaghan, M. D., Wang, Y. B. & Liao, X. Z. (2012). *Scr. Mater.* **67**, 752–755.

Wang, Y. B., Ho, J. C., Cao, Y., Liao, X. Z., Li, H. Q., Zhao, Y. H., Lavernia, E. J., Ringer, S. P. & Zhu, Y. T. (2009). *Appl. Phys. Lett.* **94**, 091911.

Williamson, G. K. & Smallman, R. E. (1956). *Philos. Mag.* **1**, 34–46.

Zhao, Y. H., Liao, X. Z., Jin, Z., Valiev, R. Z. & Zhu, Y. T. (2004). *Acta Mater.* **52**, 4589–4599.